An In-situ Bifacial Passivation Strategy for Flexible Perovskite Solar Module with Mechanical Robustness by Roll-to-roll Fabrication

Hongyu Wang[a], Zengqi Huang[b], Shuqin Xiao[a], Xiangchuan Meng[b], Zhi Xing[b], Li Rao[a], Chenxiang Gong[b], Runsheng Wu[c], Ting Hu [a,b], Licheng Tan[b], Xiaotian Hu*[a,b], Shaohua Zhang*[a], Yiwang Chen*[b,d]

[a.] *School of Materials Science and Engineering, Nanchang University, 999 Xuefu Avenue, Nanchang 330031, China.*
[b.] *College of Chemistry//Institute of Polymers and Energy Chemistry, Nanchang University, Nanchang 330031, P. R. China.*
[c.] *School of New Energy Science and Engineering, Xinyu University, Xinyu 338004, China*
[d.] *Institute of Advanced Scientific Research (iASR), Jiangxi Normal University, 99 Ziyang Avenue, Nanchang 330022, China.*

Correspondence should be addressed to C. Y., H. X. and Z. S (email: ywchen@ncu.edu.cn, happyhu@ncu.edu.cn & shz@ncu.edu.cn).

Experimental

NiO_x NPs synthesis. Nickel oxide (NiO_x) nanocomposites (NPs) were synthesized via a previously reported procedure. Nickel(II) nitrate hexahydrate ($Ni(NO_3)_2 \cdot 6H_2O$, 0.5 mol, Sigma-Aldrich, 99.999%) was dissolved in 100 mL of deionized water. Then, a sodium hydroxide (NaOH) solution (10 mol/L) was added slowly into the solution to adjust the pH to 10. After stirring for 10 minutes, the colloidal precipitate was thoroughly cleaned with deionized water. Next, the colloidal precipitate was dried at 80 °C for 6 h and then grinded to powder. Finally, the obtained colloidal precipitation was calcined at 270 °C for 2 h to obtain a dark-black powder. The NiO_x NPs were prepared by dispersing the obtained NiO_x powder in deionized water at the desired concentrations.

Preparation of HTL on rigid and flexible substrate. Glass/ITO and PET/ITO were ultrasonically cleaned with acetone, abstergent aqueous, deionized water and isopropyl alcohol for 20 min, and then blown dry by nitrogen (N_2) and treated with air plasma for 15 minutes. To fabricate rigid devices, a ~30 nm NiO_x film was fabricated by meniscus-coating a solution containing NiO_x (20 mg/mL) in deionized water (the blading speed is 10 mm $s^{-1}$and the distance between meniscus and substrate is 50 μm). And The heating temperature was 55°C. Then, the NiO_x coated substrates were annealed at 120 °C for 30 min in air. To fabricate flexible devices and for mechanical bending measurements, a highly conductive PEDOT:PSS (Heraeus CLEVIOS™ PH1000) aqueous solution with 5 wt% glycol and 0.5 wt% FS-300 was printed onto the PET substrates by meniscus-coating (the blading speed is 10 mm $s^{-1}$and the distance between meniscus and substrate is 40 μm), and subsequently annealed at 100 °C for 15 min. Then we used the same process as above to fabricate NiO_x film. And it is worth noting that the key to fabricate efficient flexible PSCs is to ensure the flatness of the flexible substrate during the device fabrication process. After the NiO_x film is fully annealed, the surface is treated with the optimal concentration of HI (0.6 wt%,Sigma-Aldrich). Because the NiO_x film layer is thin, the HI solution can slightly penetrate into the hc-PEDOT:PSS electrode, thereby playing a role in acidification and optimizing the conformation of PEDOT:PSS.

Fabrication of perovskite solar cells. The one-step perovskite solution is prepared by dissolving 547 mg PbI_2 (99.999% purity, Afar Aesar), 46 mg $PbBr_2$ (Sigma-Aldrich), 150 mg FAI (Xi'an p-OLED Corp), 39 mg MAI (>98% purity, Dyesol) and 0.02wt% PU (Sigma-Aldrich) in 1.5 mL anhydrous DMF and 1.5 mL anhydrous DMSO mixture solvent in glovebox. The perovskite precursor solution is meniscus-coated on the HTL-coated substrates (the blading speed is 10 mm $s^{-1}$and the distance between scraper and substrate is 100 μm). Before the film is annealed, it needs to be vacuum pretreated (vacuum degree below 20 Pa, lasting three minutes). Then, the perovskite precursor coated substrate is annealed on a hot plate at 150 ℃ for 15 min. Subsequently, the $PC_{61}BM$ (20 mg/ml in anhydrous chlorobenzene) and BCP (0.5 mg/ml in anhydrous ethanol) are deposited by meniscus coating, sequently. After drying, the device was completed with the evaporation of Ag contact electrodes (90 nm for small solar cells and 120 nm for solar modues) in a high vacuum level of 1×10^{-7}Torr through shadow masks. The preparation process of the test samples is the

same as that of the device preparation before evaporation.

R2R Fabrication of all-printing PSCs. The R2R printing was carried out on a GTB150B-0602E multifunctional printing machine from Shenzhen Shining Automation Equipment Co. Ltd. (China). The details of the R2R machine and process are shown in **Figure 17**. The process was performed with tension control to drive the web at fixed speed. The winding tension and slit spacing are determined to be 45 N and 200 μm respectively, air shower is carried out on the printed active layers (The air shower intensity is 0.1 bar). Before the device fabrication, PET/ITO or PET substrate were treated by ultrasonic cleaning with acetone, deionized water and isopropanol. After that, a corona treatment was used to clean and control the wettability. The hc-PEDOT:PSS transparent electrode was slot-die printed based on our previous work[1].

The NiO_x films were obtained by slot-die with the tape speed of 0.20 m/min, inking speed of 0.25 ml/min and slit spacing of 200 μm, following by annealing at 120℃ for 20 min. After the films were completely dry, immerse it in-situ with HI solution (0.6wt%) for 10s and annealed at 80 ℃ for another 10 minutes. Meanwhile, in order to illustrate whether the interface nickel iodide (NiI_2) can be dissolved in the perovskite precursor, the solubility of NiI_2 in DMF was explored, as shown in **Figure S23**. the solubility of NiI_2 in DMF is very small and it will be further reduced during the printing process due to the amount of solution. To further illustrate the problem, we conducted SEM-EDX maps to analyze the element distribution on the surface of the NiO_x (HI) film with and without (DMF) modification (**Figure S24**). The element content on the surface of the film did not change significantly, and the dissolution of NiI_2 on the surface of the perovskite precursor can be ignored.Then the active layer of PSCs was fabricated by slot-die process with the one-step perovskite solution above. Because of the synergistic of air shower and annealing, the thickness of active layer is about 300-450 nm, and it will not change obviously with the change of printing parameters. Then, the sample was transferred to the air knife and purged with nitrogen for 3 min to remove the solvent. Subsequently, the samples were immediately annealed at 100 ℃ for 10 min for testing and characterization. Finally, the $PC_{61}BM$ (20 mg/ml in anhydrous chlorobenzene) and BCP (0.5 mg/ml in anhydrous ethanol) were deposited by meniscus coating, sequently. After drying, the device was completed with the evaporation of Ag contact electrodes (90 nm for small solar cells and 120 nm for solar modues) in a high vacuum level of 1×10^{-7}Torr through shadow masks.

Fabrication of perovskite solar modules. The fabrication process of PSMS is identical to that of small area optoelectronic devices, but their effective areas are different. The solar module was consisted with 6 sub-cells and the size of a single cell is 2.5 cm^2 (0.8 cm×3.1 cm), respectively. All the scribing techniques are performed by the rectification unit, the dislocation of each layer is about 0.2 cm. In addition, the module interconnection illustration is shown as below. No further encapsulation was performed on perovskite solar cells and modules.

Film characterizations. The morphology of films was measured by SEM (JEOL, JSM-7500F, 104 Japan) at an accelerating voltage of 5.0 kV and AFM (nanoscope multimode Bruker).X-ray diffraction (XRD) and 2D-XRD measurements were

recorded by using a D8-Discover 25 diffractometer (Bruker). The steady-state photoluminescence (PL) and time-resolved photoluminescence (TRPL) measurements at the peak emission of ~ 680 nm (on the excitation at 550 nm) were carried out by a steady state and lifetime spectrometer (FLS920, Edinburgh Instruments Ltd.). The TRPL excitation fluence is ≈4 nJ cm^{-2} from a 405 pulsed laser with a wavelength of 405±8 nm and pulse width of 45 ps, at a repetition rate of 0.1 MHz. The PL decay data was recorded using time-correlated single photon counting technique. The ultraviolet-visible (UV-Vis) spectra are recorded by SHIMADZU, UV-2600 spectrophotometer. XPS studies were performed on a Thermo-VG Scientific ESCALAB 250 photoelectron spectrometer using a monochromated AlKa (1486.6 eV) X-ray source. All recorded peaks were corrected for electrostatic effects by setting the C−C component of the C 1s peak to 284.8 eV. The base pressure in the XPS analysis chamber was 2×10^{-9} mbar. The dual-beam ToF-SIMS depth profiling measurements were performed on a ToF-SIMS 5 instrument (ION-TOF GmbH) in an interlaced mode. A pulsed 30 keV Bi^{+} ion beam was used as the analysis beam with the beam current of 1.08 pA.

Solar cells characterizations. The electrical impedance spectroscopy (EIS) was tested at Zahner electrochemical workstation. The current density-voltage (J-V) and current-voltage (I-V) curves were characterized using Keithley 2400. The illuminated currents were measured under the simulated 100 mW cm^{-2} and AM 1.5 G irradiation (Enli Tech). The reference silicon solar cell was corrected from NREL. All measurements were performed in a nitrogen glove box. The forward scan range is from 0 V to 1.2 V and the reverse scan range is from 1.2 V to 0 V, with 8.0 mV for each step. The scan rate is 200 mV s^{-1} and the delay time is 30 ms. The incident photon-to-current conversion efficiency (IPCE) spectra were detected under monochromatic illumination (Oriel Cornerstone 260 1/4 m monochromator equipped with Oriel 70613NS QTH lamp), and the calibration of the incident light was performed with a monocrystalline silicon diode. The repeated bending cycle tests were completed by a stretching machine (Beijing Zhongke J&M). All the results of bending test were averaged from over 100 samples.

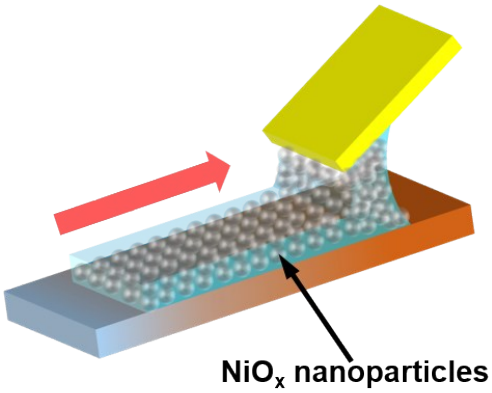

Fig. S1. The schematic diagram of fabricating NiO_x film by blade coating.

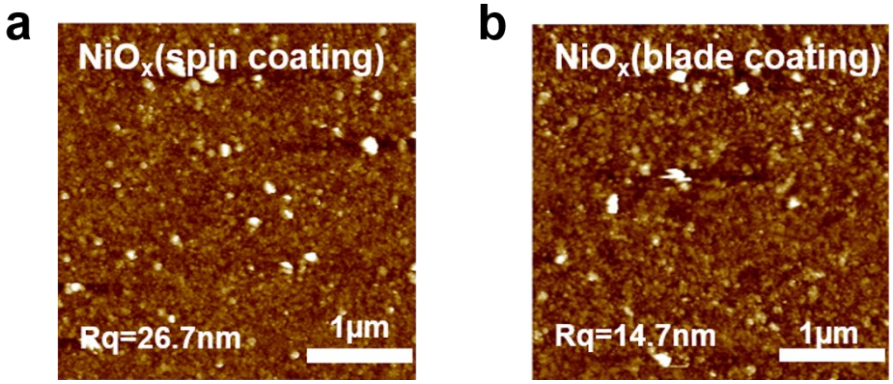

Fig. S2. Atomic force microscopy (AFM) images of NiO_x film based on spin-coating and blade-coating process. The film morphology becomes smoother by blade-coating process.

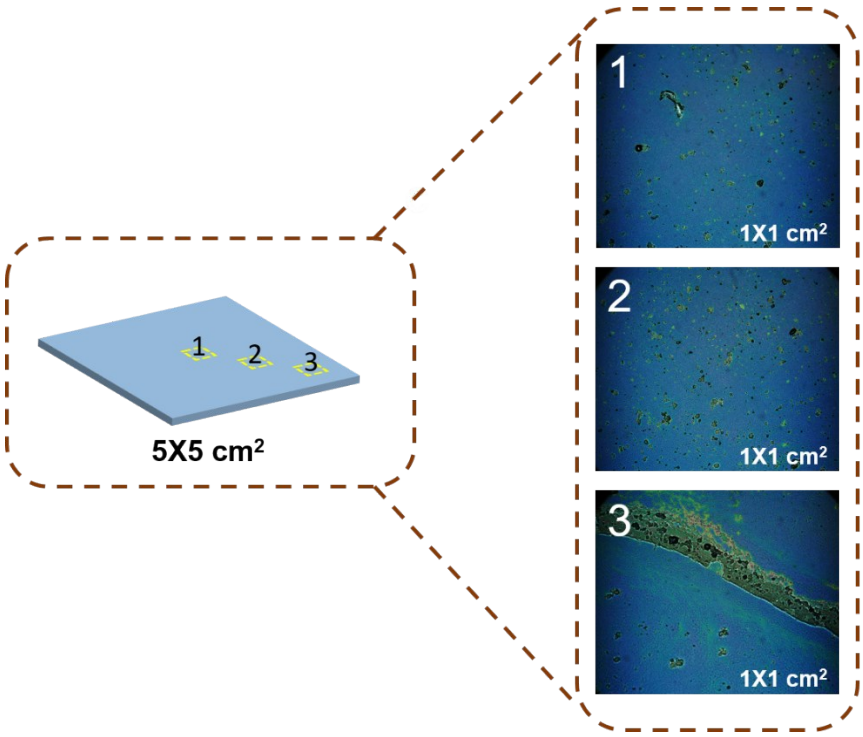

148

149

150 **Fig. S3.** Optical microscope (OM) images of NiO_x nanoparticles spin-coated on a
151 rigid substrate of 25 cm^2. Areas 1, 2 and 3 are the measuring selection.

152

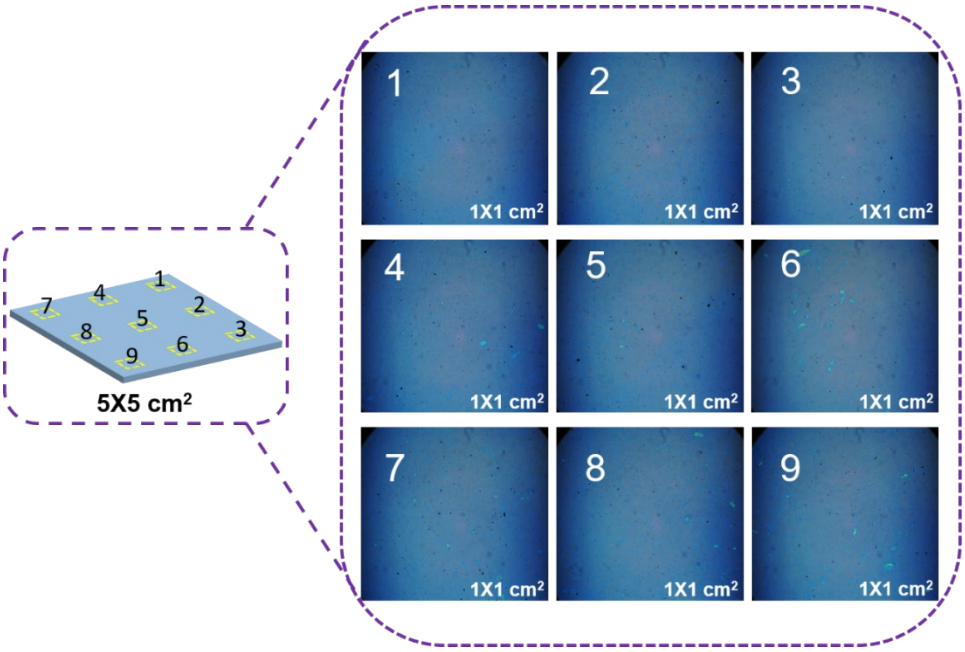

Fig. S4. Optical microscope (OM) images of NiO_x nanoparticles spin-coated on a rigid substrate of 25 cm^2. Areas 1-9 are the measuring selection.

In order to prove that the blade-coating process is more conducive to the formation of a uniform NiO_x film than the spin-coating process, atomic force microscopy (AFM) and optical microscopy (OM) are detected to characterize the morphology of the NiO_x films. The NiO_x films are deposited on a rigid substrate of 25 cm^2. As shown in **Figure S2**, the NiO_x films fabricated by blade-coating process present smooth surface roughness, and its surface roughness value (14.7nm) is about half that (26.7nm) of the films fabricated by spin-coating process. This result indicates that the NiO_x nanoparticles will be distributed on the substrate in an orderly manner due to the solution shear force during the blade-coating process, thereby obtaining a uniform and flat film. In addition, to prove the above conclusion more intuitively, optical microscope (OM) images of the surface of the NiO_x film are collected. In order to reflect the reliability of the data, the different selected areas (1cm^2) of the NiO_x film are measured. As shown in **Figure S3** and **S4**, the NiO_x film fabricated by spin coating has obvious aggregation outside the central area. On the contrary, the film fabricated by blade coating is relatively uniform on the entire substrate. This consequence is consistent with the data analysis of AFM. Thus, it is easier to prepare a large-area uniform film by the blade-coating process, which endows the basis for enhanced performance of large-area PSCs.

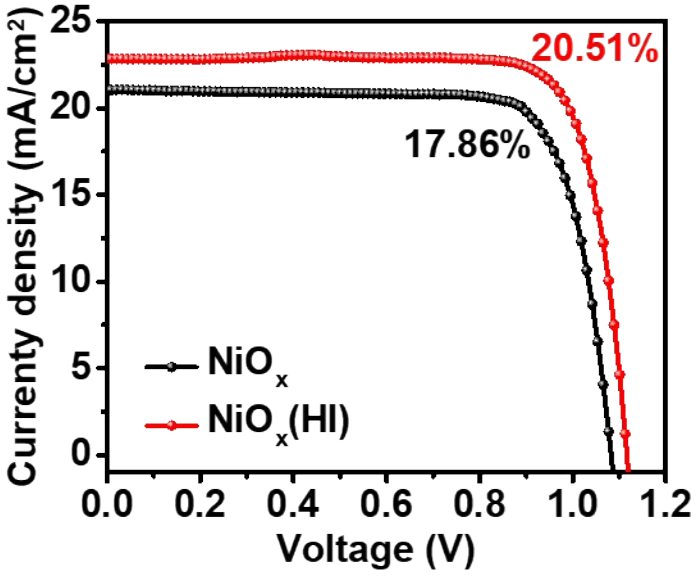

Fig. S5. Typical *J-V* curves of a small area rigid device based on NiO_x and NiO_x (HI) HTLs. A significant PCE improvement can be observed when using the optimal concentration (0.6wt %) of HI solution treats on the NiO_x film.

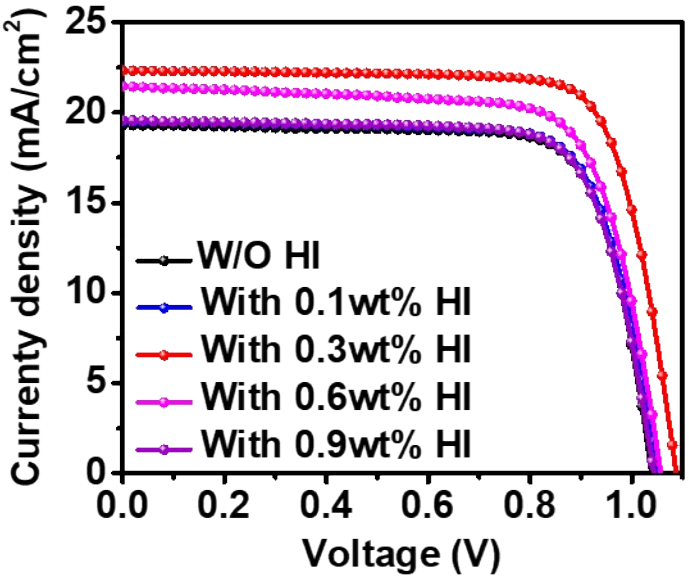

Fig. S6. Typical *J-V* curves of PSCs based on different concentration of HI solution treated NiO_x film.

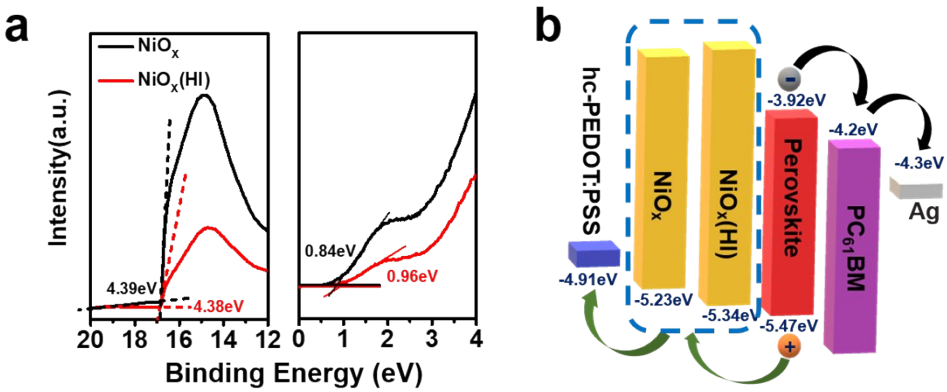

185

186 **Fig. S7.** a) Ultraviolet photoelectron spectroscopy (UPS) spectra for NiO_x films with
187 and without HI surface modification. b) Energy level diagram of the perovskite solar
188 cells (data for the corresponding NiO_x films and perovskite layers are provided by
189 UPS measurement).

190

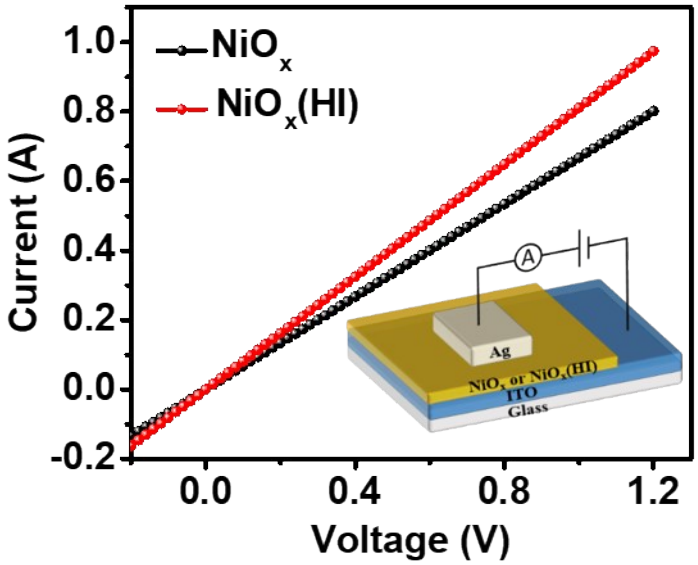

Fig. S8. The current-voltage (*I-V*) plots of hole only devices with unmodified and HI-modified NiO_x hole extraction layers. The inset shows the device structures: ITO/NiO_x/Ag or ITO/NiO_x (HI)/Ag.

We determined the conductivity of the NiO_x films by the following equation:

$$\sigma = D/(AR) \quad (1)$$

Where σ is the conductivity, A is the active area (1×1 cm^2), D is the thickness of the film, and R is the resistance obtained from the current-voltage (*I-V*) curves.[2]

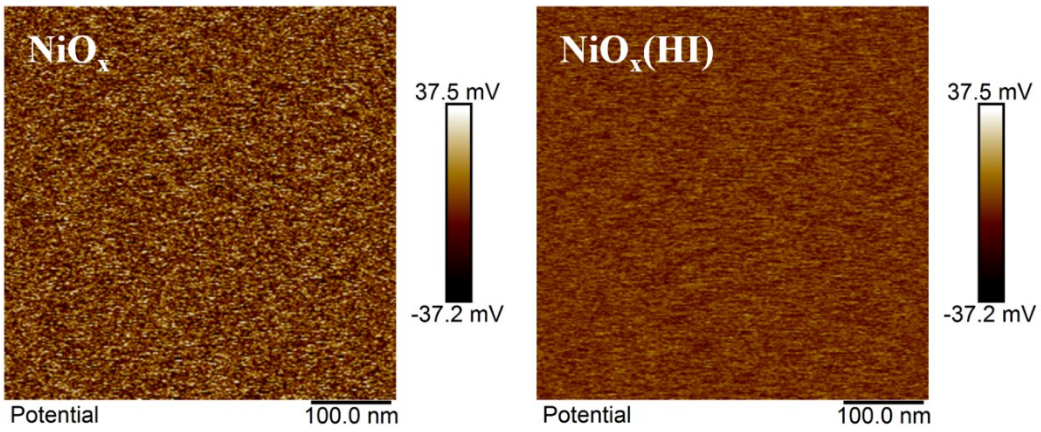

Fig. S9. Kelvin probe force microscopy (KPFM) images of NiO_x films without and with HI surface modification.

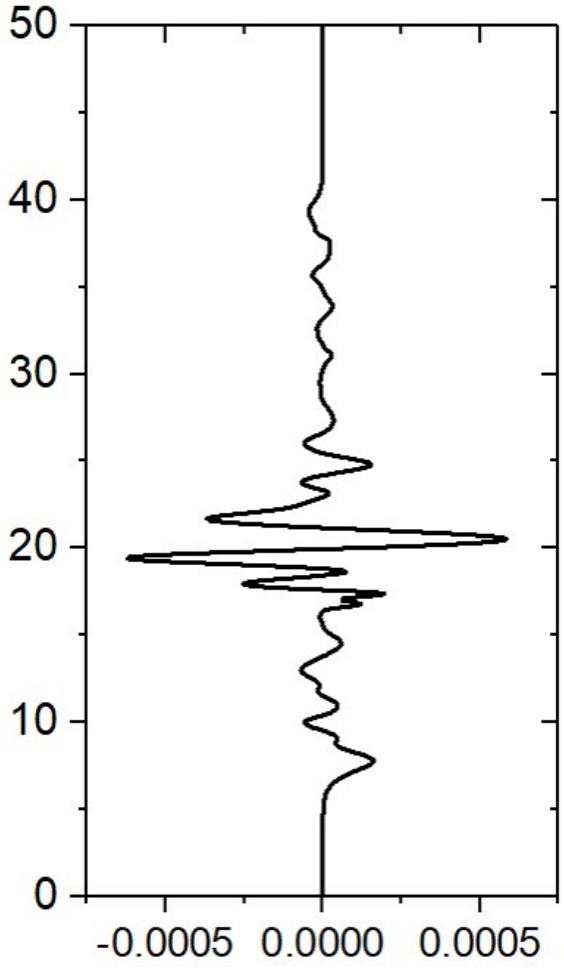

Fig. S10. Integration of Δρ in planes parallel to the surface and plotted as a function of the z coordination. Δρ represents the differential charge density, and its calculation formula is as follows: $\Delta\rho = \rho$ (perovskite /NiI_2) - ρ (perovskite) - ρ (NiI_2).

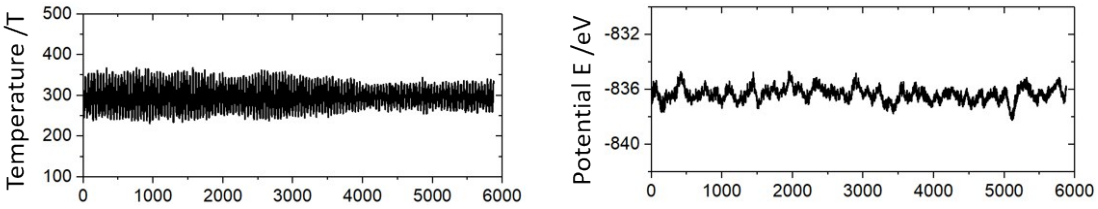

Fig. S11. Variations of temperature and energy against the time for AIMD simulations of NiI_2/perovskite.

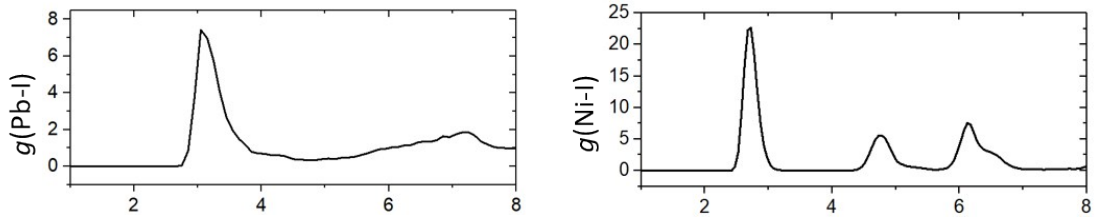

Fig. S12. Radical distribution function of Pb-I and Ni-I.

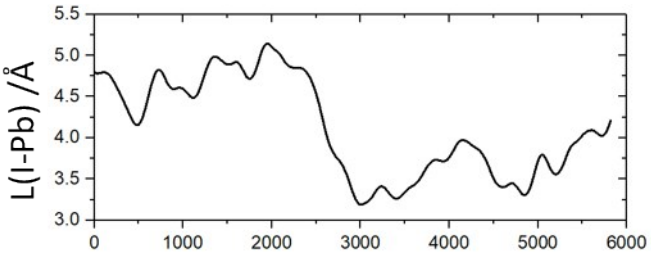

Fig. S13. The Pd-I bond pair distance against the time for AIMD simulations.

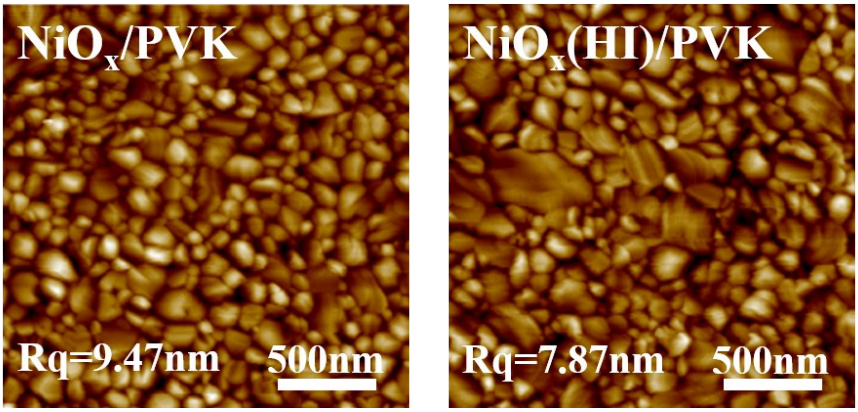

Fig. S14. Atomic force microscope (AFM) images of perovskite films based on NiO_x and NiO_x (HI) as hole transport layer (HTL).

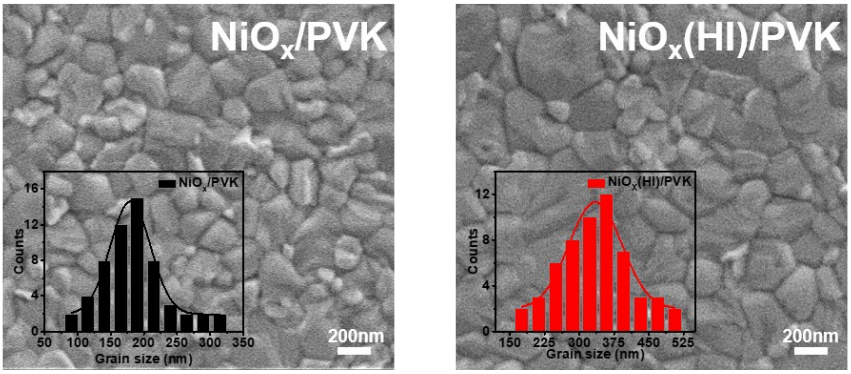

Fig. S15. The top-view SEM images of flexible perovskite films based on NiO_x and NiO_x (HI) HTL. The embedded histogram shows the distribution of the corresponding perovskite grain size.

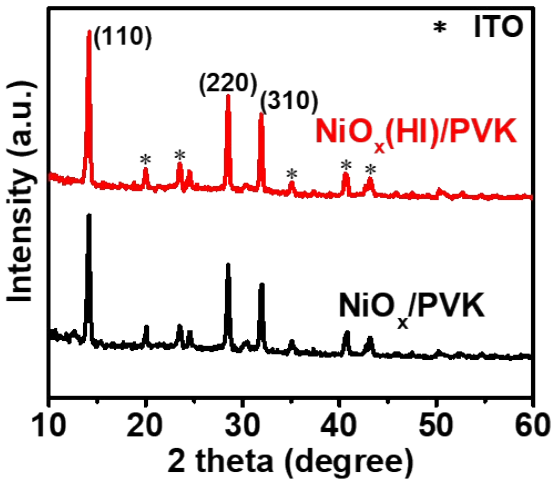

230

231 **Fig. S16** X-ray diffraction (XRD) patterns of NiO_x films with and without HI
232 treatment.

233

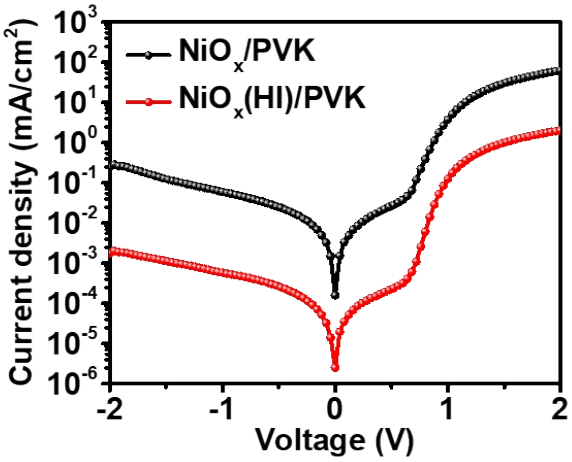

Fig. S17 Dark *J-V* curves of the PSCs for NiO_x and NiO_x (HI) as HTL.

As shown in Figure S15, dark *J-V* curves are characterized to investigate the transport performance of photogenerated carriers. the lower dark current density for the device based on HI interface modification indicates that the more photogenerated carriers can be transmitted efficiently through the perovskite films rather than directly diverged, which results in the effective suppression of charge carrier recombination and leakage current. The above results suggest that HI interface modification can indeed reduce the trap-assisted bimolecular recombination, which also means the better perovskite film quality and interfacial ohmic contact.

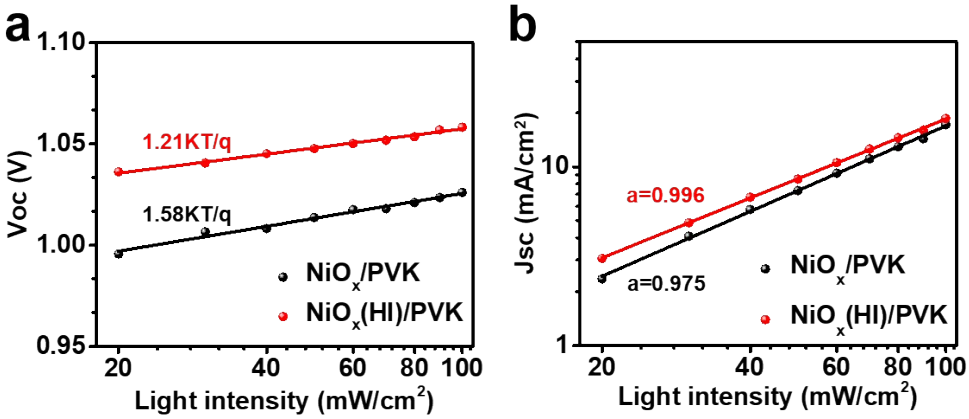

Fig. S18. a) *V*oc and b) *J*sc dependence of the PSCs prepared on NiO_x and NiO_x (HI) substrates at various illumination intensities.

Then, the details of carrier recombination are further investigated by measuring *J-V* curve under various illumination intensities. The slope of V_{oc} versus illumination intensity produced *kT/q* (where k is the Boltzmann constant, T is the temperature in kelvin, and q is the elementary charge).[3] As shown in **Figure S16a** (Supporting Information), the slope of the device decreases from 1.58 *kT/q* (reference) to 1.21 *kT/q*, which indicates that the trap-assisted recombination is effectively reduced under open-circuit conditions. Accordingly, the power law dependence of J_{sc} on the illumination intensity can be defined as J_{sc}-I^{α} (where *I* and α are the light intensity and exponential factor, respectively) (**Figure S16b**, Supporting Information).[2] The value of α for the HI-treated device (0.996) is higher than those of the reference device (0.975), demonstrating a reduction in the bimolecular recombination under short-circuit conditions.

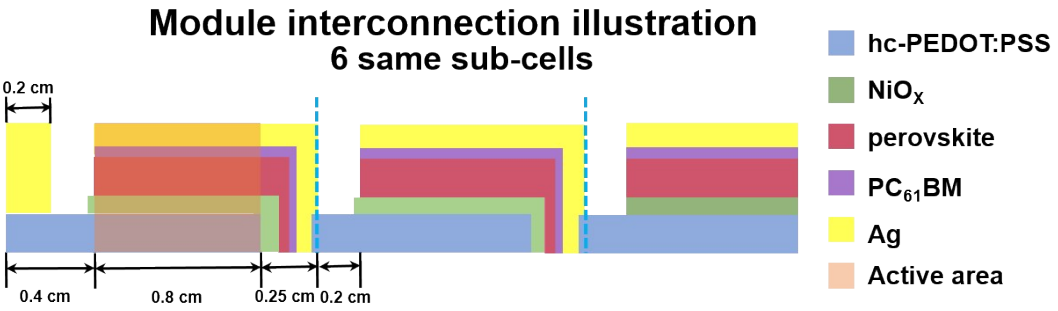

Fig. S19. The structure of perovskite solar modules.

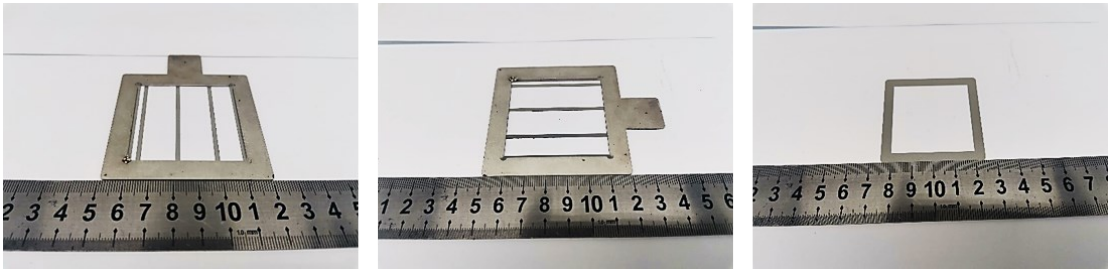

Fig. S20. The mask plate for device vapor deposition of silver and the shading plate for *J-V* curve measurement. These are used to determine the effective area of the large area module.

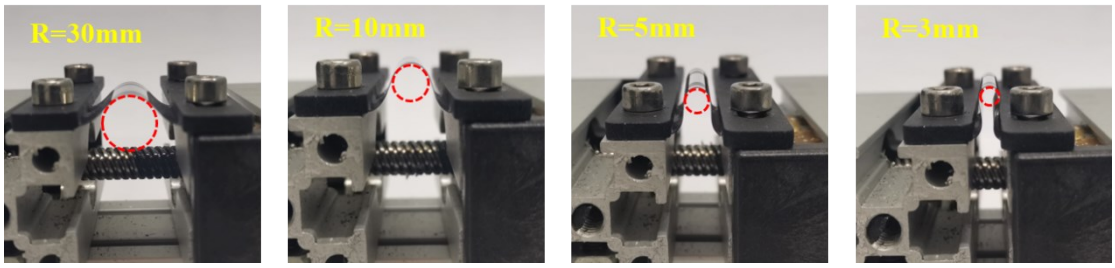

Fig. S21. Photographs of flexible devices under different bending radii.

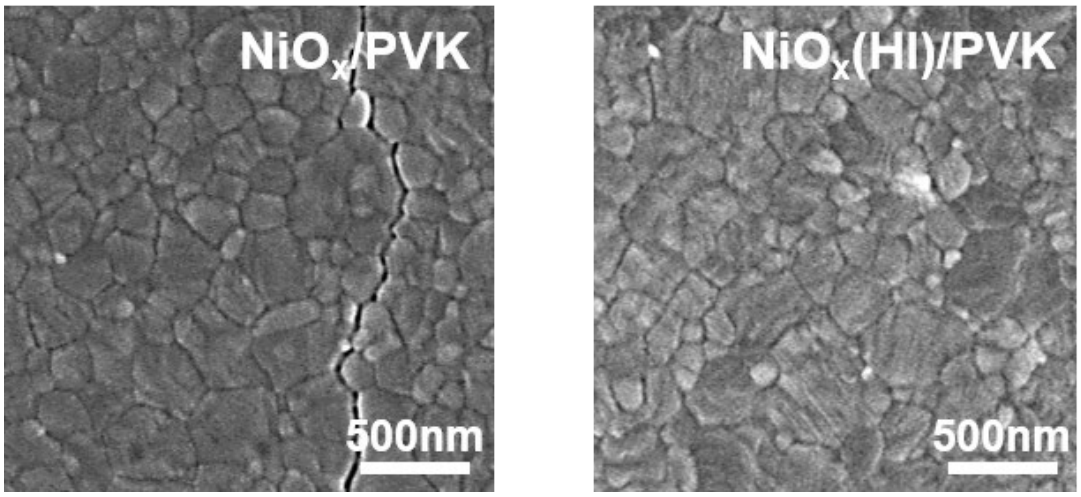

Fig. S22. The top-view SEM images of the flexible device after 5000 bends under a bending radius of 3mm. The devices without HI acid treatment of the NiO_x film show obvious cracks. On the contrary, the devices with NiO_x (HI) as the HTL do not produce obvious cracks.

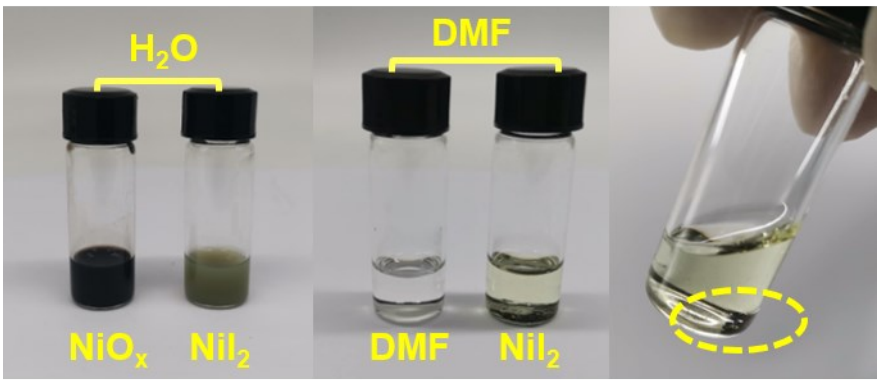

Fig. S23. Photographs of the solubility of nickel iodide (NiI_2) in water and DMF.

As shown in Figure S23, the solubility of NiI2 in DMF is very small and it will be further reduced during the printing process due to the amount of solution. To further illustrate the problem, we SEM- EDX maps to analyze the element distribution on the surface of the NiOx (HI) film with and without (DMF) modification (Figure S24). The element content on the surface of the film did not change significantly, and the dissolution of NiI2 on the surface of the perovskite precursor can be ignored.

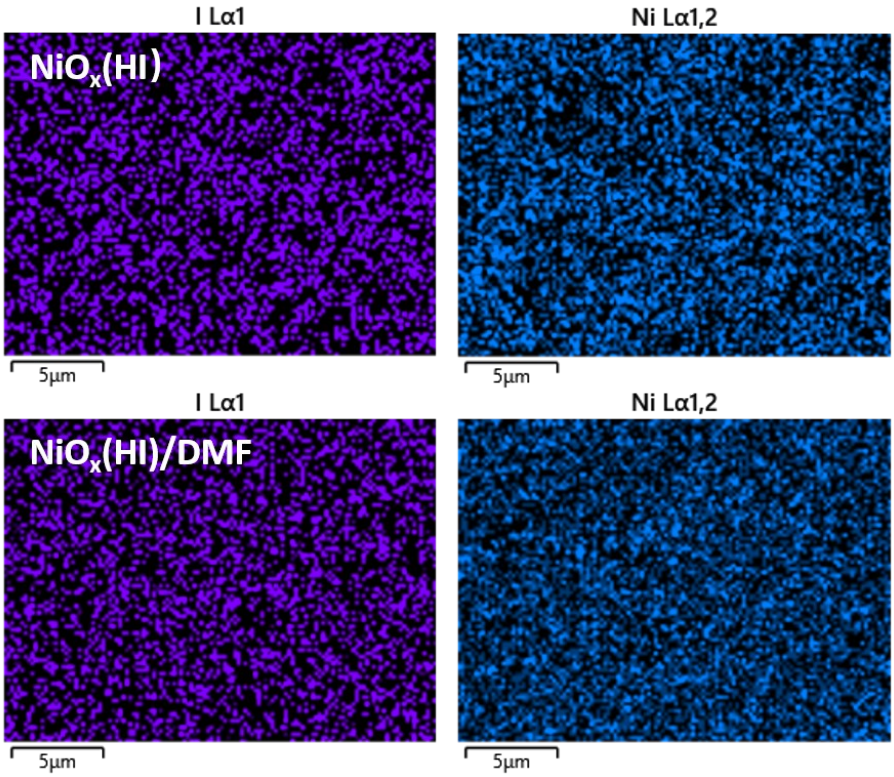

Fig. S24. SEM- EDX maps of I and Ni elements for NiO_x (HI) film with and without N, N-Dimethylformamide (DMF) modification.

Fig. S25. Photographs of roll-to-roll printing machine and main processing components in the printing process.

Table S1. The parameters derived from the typical *J-V* curves of flexible PSCs based on different concentration of HI treated NiO_x substrates.

Device	V_{oc} (V)	J_{sc} (mA/cm^2)	FF (%)	PCE (%)
NiO_x	1.04	19.31	76.58	15.38
NiO_x (HI 0.1 wt%)	1.04	19.57	75.76	15.48
NiO_x (HI 0.3 wt%)	1.04	19.52	76.66	15.57
NiO_x (HI 0.6 wt%)	1.09	22.32	78.26	19.04
NiO_x (HI 0.9 wt%)	1.06	21.45	73.52	16.72

Table S2. The parameters derived from the typical *J-V* curves of flexible PSCs based on 0.6 wt% HI treated NiO_x substrates.

Device		V_{oc} (V)	J_{sc} (mA/cm^2)	FF (%)	PCE (%)
NiO_x	forward	0.96	19.33	76.10	14.15
	reverse	1.04	19.31	76.59	15.38
	Average	1.01±0.04	19.11±0.24	76.10±0.51	14.56±0.85
NiO_x (HI)	forward	1.09	22.14	77.89	18.80
	reverse	1.09	22.32	78.26	19.04
	Average	1.07±0.02	22.12 ±0.21	77.90±0.37	18.62±0.43

The average and standard deviation values are based on 50 cells and the "±" is defined as the error bar.

Supplementary Note 1.

Gibbs free energy theory for judging the progress of chemical reactions: the corresponding chemical reaction equation is as follows:

$Ni(OH)_2$ (s) + HI (l) → NiI_2 (s) + H_2O (l) (1)

Ni_2O_3 (s) + HI (l) → NiI_2 (s) + H_2O (l) + I_2 (g) (2)

NiOOH (s) + HI (l) → NiI_2 (s) + H_2O (l) + I_2 (g) (3)

The first equation is the acid-base neutralization reaction. Nickel hydroxide is a reducing hydroxide, which has strong alkalinity and can be dissolved in acid. Moreover, according to the Gibbs free energy calculation formula:

$\Delta G = \Sigma\Delta G_1 - \Sigma\Delta G_2$

where $\Sigma\Delta G_1$ represents the sum of Gibbs free energy of each product, and $\Sigma\Delta G_2$ represents that of each reactant, the calculated value of ΔG is -185.988 kJ mol^{-1} ($\Delta G<0$), indicating that the reaction can proceed forward.

In reaction equations 2 and 3, trivalent nickel ions have strong oxidizing properties and can rapidly undergo oxidation-reduction reactions with acid radical ions in water. In addition, the progress of the reaction can also be judged by the Gibbs free energy calculation formula:

$\Delta G = \Delta H - T\Delta S$

where ΔH represents the enthalpy change of the reaction, T is the reaction temperature, and ΔS represents the entropy change of the reaction. Calculated according to the query chemistry manual, the enthalpy change values (ΔH) of reactions 2 and 3 are correspondingly -609.24 kJ mol^{-1} and -559.3 kJ mol^{-1} ($\Delta H<0$). At the same time, according to the physical meaning of entropy, it can be known that the entropy value is related to the disorder of the reaction system. Reactions 2 and 3 both emit gas based on redox reactions, indicating that the disorder of the system is increasing, that is, the entropy value increases ($\Delta S>0$). Therefore, according to the above Gibbs free energy formula, it is judged that the ΔG values of reactions 2 and 3 are negative ($\Delta G<0$), indicating that the above reactions can proceed in a positive direction.

References

1. X. Hu, Z. Huang, X. Zhou, P. Li, Y. Wang, Z. Huang, M. Su, W. Ren, F. Li, M. Li, Y. Chen, Y. Song, *Adv. Mater*. 2017, **29**, 1703236.
2. B. Parida, S. Yoon, J. Ryu, S. Hayase, S. M. Jeong, Dong-Won Kang, *ACS Appl. Mater. Interfaces.* 2020, **12**, 22958.
3. V. D. Mihailetchi, H. Xie, B. Deboer, L. J. A. Koster, P. W. M. Blom, *Adv. Funct. Mater.* 2006, **16**, 699.